



# Critical assessment of the determination of residual stress profiles in thin films by means of the ion beam layer removal method



R. Schöngrundner<sup>a,\*</sup>, R. Tremel<sup>b</sup>, T. Antretter<sup>c</sup>, D. Kozic<sup>a</sup>, W. Ecker<sup>a</sup>, D. Kiener<sup>b</sup>, R. Brunner<sup>a</sup>

<sup>a</sup> Materials Center Leoben, Roseggerstrasse 12, Leoben, Austria

<sup>b</sup> Department of Materials Physics, Montanuniversität Leoben, Jahnstrasse 12, Leoben, Austria

<sup>c</sup> Institute of Mechanics, Montanuniversität Leoben, Franz-Josef-Straße 18, Leoben, Austria

## ARTICLE INFO

### Article history:

Received 10 February 2014

Received in revised form 26 May 2014

Accepted 2 June 2014

Available online 9 June 2014

### Keywords:

Ion beam layer removal

Residual stress profile

Tungsten

Titanium nitride

Thin films

Finite element modeling

Optimization

## ABSTRACT

Residual stresses and their distribution within individual layers are a general concern in thin film technology. Here we use a recently developed ion beam layer removal method to determine the stress profile in a thin film system. The system consists of a thin tungsten and titanium nitride film deposited on a silicon substrate. The stresses are calculated from the deflection of a focused ion beam machined cantilever by means of Euler–Bernoulli beam theory and finite element simulations coupled with optimizing algorithms, and the results of the two methods are critically compared. Case studies taking into account manufacturing related variations in the cantilever geometry, different boundary conditions and relaxation during cantilever fabrication are performed. We find that the stress distribution in the thin film system is strongly influenced by the boundary conditions and the cantilever fabrication, while manufacturing related variations in the cantilever geometry only slightly influence the stress distribution.

© 2014 The Authors. Published by Elsevier B.V. This is an open access article under the CC BY-NC-ND license (<http://creativecommons.org/licenses/by-nc-nd/3.0/>).

## 1. Introduction

The investigation of local residual stresses is important since they can affect the functionality and lifetime of many components. Residual stresses may occur due to plastic deformation, phase transformation, coating deposition or other inelastic processes. They can be found in bulk materials as well as in thin films across the entire length scale, starting from e.g. large manufacturing tools like casting dies with several meters in dimension down to nano-scale-structures used in the microelectronics industry, e.g. micro-electro-mechanical systems (MEMS) [1]. In the latter, especially multilayer and multi-material systems can show relatively high residual stresses due to elastic or thermal mismatch [2–5]. To assess the risk of component failure it is necessary to investigate the local distribution and evolution of stresses in such devices.

In recent years, a number of methods were developed to study residual stresses in components and structures. Most of these methods determine the residual stresses globally, e.g. using wafer curvature [6, 7] or X-ray diffraction (XRD) [1,8–11] techniques, assuming a homogeneous stress distribution and no significant stress gradient over the investigated thickness. However, residual stresses are usually not distributed homogeneously. Therefore other methods such as grazing incidence X-ray [7] or X-ray nano-beam techniques [12,13] have been

developed. These methods allow a depth resolution on the nano-scale, however only for crystalline materials. Another method resembles focused ion beam (FIB) milling in combination with digital image correlation (DIC). During FIB milling the material in the vicinity of the cut relaxes its internal stresses, leading to deformation, which can be measured by applying DIC. Subsequently, the stresses are calculated from the deformation field using a finite element (FE) calculation or analytical approaches. Different geometries, such as circular holes [14,15], rectangular trenches [16–18], pillars [19] or H-bars [20] are used to determine residual stress profiles. However, several DIC based methods require a sufficiently structured surface on the material under investigation to assure enough homologous points in order to determine the deformation field in a reliable manner. Other disadvantages of the mentioned methods are related to certain aspects of the FIB milling or the stress analysis [20,21].

In the case of holes or trenches, the significant strain relief is always located near the milled region which results in a very complex and non-linear strain gradient. Consequently, a FEM analysis is needed to calculate the residual stresses from the measured strains. Furthermore, the strain relief lies within the FIB damaged region which can influence the deformation behavior of the material. The H-bar shape also requires a FEM analysis to determine the residual stresses. The pillar geometry overcomes these problems, but has the drawback of small deformations, leading to inaccurate results especially for low residual stresses. Furthermore, the use of complex geometrical shapes may represent a critical issue for FIB instruments that deploy a raster-based patterning

\* Corresponding author. Tel.: +43 3842 45922 40; fax: +43 3842 45922 500.  
E-mail address: [r.schoengrundner@mcl.at](mailto:r.schoengrundner@mcl.at) (R. Schöngrundner).

engine for the movement of the ion-beam. However as shown e.g. in [19,22] the application of a vector-based patterning engine solves this problem enabling the reliable processing of complex geometries like circular or ring shaped trenches.

A promising approach to overcome the above listed restrictions and disadvantages is the so-called ion beam layer removal (ILR) method in combination with an analytical stress calculation [23–26]. This technique allows the evaluation of the stress distribution over the film thickness by using micro-scaled cantilever bending experiments. The ILR method makes use of the idea that the deflection of a cantilever depends on the distribution of residual stresses within the film. The deflection can be easily measured using scanning electron microscopy (SEM) and does not require any DIC or surface structure per se. However, the resolution accuracy could be substantially further improved by a combination of both approaches. The analytical approach can be used to estimate the residual stress distribution from the deflection of the cantilever. While the combination of ILR with an analytical approach provides a simple estimate of the residual stress distribution, the influence of real cantilever geometries deviating from idealized shapes, realistic boundary conditions, as well as stress relief during cantilever fabrication is not taken into account. Until now, it is unclear how these parameters affect the calculated residual stress distribution. In this paper, the ILR method is used in combination with analytical and numerical calculations in order to study the influence of the mentioned parameters on the stress distribution in thin films to further improve the ILR method. Therefore, we evaluate the residual stress in a multilayer thin film sample consisting of a thin tungsten (W) film and a thin titanium nitride (TiN) interlayer deposited on single crystalline silicon (Si) substrate (wafer). The different thin films investigated here are, for example, used in microelectronic devices [27].

## 2. Description of the ILR method

A recently developed ILR method [23–26] is used to determine the residual stress profile in the multilayer film system. The calculation method is based on the standard Euler–Bernoulli beam theory [28], which provides means to calculate the load-carrying and deflection characteristics of beams. It covers the case for small deflections of a cantilever that is subjected to lateral loads. Residual stresses inside the film lead to a deflection of the cantilever. This deflection depends on the initial residual stress, the film and substrate thickness, the momentum of inertia of the cantilever as well as on the Young's moduli of the materials involved. In principle the ILR method works as discussed in the following paragraphs.

In the first step a cantilever, which is fixed on both sides, is fabricated with a FIB workstation out of the initial system in the vicinity of the sample edge, see Fig. 1. In the next step the supporting material on one side of the cantilever is removed. This leads to a positive or negative deflection, depending on the residual stress distribution in the system. The first deflection (surface to surface distance) is measured with a scanning electron microscope at the free end of the cantilever (deflection area), see Fig. 1. To determine the stress distribution across the coating, the film thickness is gradually reduced in the rear part of the cantilever (Fig. 1b; ILR area) over a width of 10–15  $\mu\text{m}$ . The milling is performed from the side of the cantilever to minimize the influence of Ga implantation [29]. The rest of the cantilever (Fig. 1b; section B) remains unaltered and acts as pointer to measure deflection changes during FIB milling. The gradual thinning of the cantilever affects the stress distribution and reduces the stiffness of the system. They both lead to a deflection change, which is again measured for every milling step at the tip of the cantilever (Fig. 1a; red dashed box). SEM images are taken after each milling step in order to determine the remaining film thickness and to measure the deflection (Fig. 1c–e). The mean stress from each removed layer, in the following termed sublayer, is determined from the actual deflection, the elastic properties of the system and the dimensions of the cantilever. The measured deflections as well

as the sublayer thicknesses are consequently used to determine the residual stresses in the sublayers by means of an analytical approach, using the Euler–Bernoulli beam theory following Jiang et al. [26]. In comparison to Massl et al. [23] this approach is more straightforward and the solution provides directly the residual stress working in the initial condition for each sublayer. In the following the procedure is explained in detail: Under the condition of small elastic deformations, the curvature  $\kappa$  of a cantilever can be calculated from its deflection curve  $u(x)$  via

$$\frac{d^2 u}{dx^2} = \kappa. \quad (1)$$

The solution of the differential equation leads to the relation between the initial deflection and the initial curvature of the entire cantilever,

$$\kappa_B = -\frac{2 \delta_{\text{original}}}{l^2}. \quad (2)$$

Here  $\kappa_B$  denotes the initial curvature of the entire cantilever after the free cut on one side,  $\delta_{\text{original}}$  denotes the first measured deflection and  $l$  is the cantilever length. During gradual film thinning, the curvature of the ILR area changes and thus the deflection of the cantilever. As the measured deflection change is, for a given length of the ILR area, a function of the actual cantilever thickness in the ILR area and the initial deflection calculated with Eq. (2), the curvature of the cantilever along the ILR area,  $\kappa_{A_i}$ , can only be determined iteratively by solving Eq. (3) for each measured deflection  $\delta_i$  [23] where  $i = 1, 2, \dots, n$  indicates the remaining system consisting of the substrate and  $n - i$  sublayers:

$$\delta_i = \frac{1}{\kappa_{A_i}} \left[ 1 - \cos(\kappa_{A_i} l_A) \right] + \sin\left(\kappa_{A_i} l_A + \kappa_B \frac{l_B}{2}\right) \frac{2}{\kappa_B} \sin\left(\kappa_B \frac{l_B}{2}\right). \quad (3)$$

$l_A$  and  $l_B$  denote the length of the ILR area and section B, see Fig. 1b.

In the next step, the stress distribution in the layer system is calculated by means of force and momentum balance over the cantilever. Each previously removed sublayer is now added in the reverse order, and the mean stresses in the sublayers are calculated with regard to the experimentally determined curvatures. Since the cantilever deflection is caused only by internal forces due to the preexisting residual stresses in each sublayer  $j$ , they can be determined by solving the following equations for the equilibrium of force,  $N$ , and moment,  $M$ :

$$N = \int_0^{t_0} \sigma_{x,0}(z) dz + \sum_{j=0}^n \int_{t_j}^{t_{j+1}} \sigma_{x,j}(z) dz = 0, \quad (4)$$

$$M_y = \int_0^{t_{\text{sub}}} \sigma_{x,0}(z) \cdot z dz + \sum_{j=0}^n \int_{t_j}^{t_{j+1}} \sigma_{x,j}(z) \cdot z dz = 0, \quad (5)$$

in which  $\sigma_{x,0}(z)$  denotes the stress distribution in  $z$ -direction in the substrate and  $\sigma_{x,j}(z)$  denotes the stress distribution in each sublayer, both for the relaxed system.  $A$  is the integration area,  $t_{\text{sub}}$  and  $t_j$  denote the substrate thickness and the actual distance from the origin of the coordinate system. The coordinate system is located at the bottom of the substrate, see Fig. 2. Because the lateral dimension of the wafer is much greater than the thickness, it is assumed that the film is under a biaxial plane stress state ( $\sigma_{x,j}(z) = \sigma_{y,j}(z)$ ) and that the biaxial stress state only slightly changes during cantilever fabrication. Simplified model cases are used to ensure that the stress relaxation in sample width is negligible for the studied system. It is found that the shown stress assumption is valid. The stresses in Eqs. (4) and (5) consist of the mechanical stress  $\sigma_{x,j}^m(z)$ , caused by the deformation of the

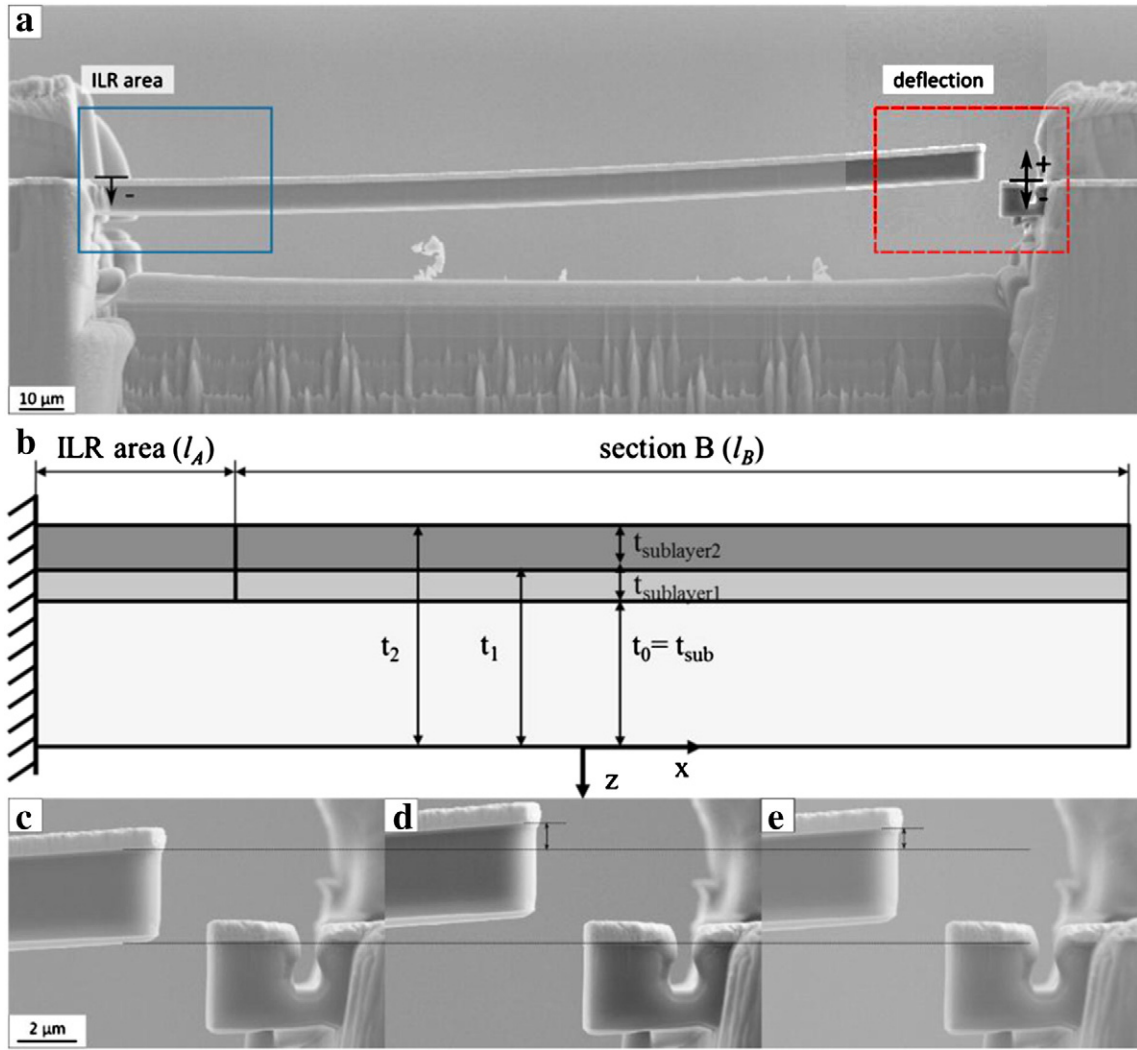


**Fig. 1.** a) SEM image of the cantilever which bends upwards due to the effect of the tensile residual stress. The blue box indicates the ILR area and the red dashed box indicates the cantilever tip where the deflection is measured. (b) Schematic drawing of the cantilever showing the dimensioning used in the numerical and analytical calculation. (c–e) Enlargements of the SEM image in (a) showing the deflection area for different FIB removal stages of 3.82, 3.97, and 3.96  $\mu\text{m}$ , respectively.

cantilever, and the eigenstress in each sublayer,  $\sigma_{x,j}^{\text{res}}$ , and can be determined from Eq. (6),

$$\sigma_{x,j}(z) = \sigma_{x,j}^m(z) + \sigma_{x,j}^{\text{res}} = (\varepsilon_{x,j}^m(z) + \varepsilon_{x,j}^{\text{res}}) \cdot E_{bj} = \varepsilon_{x,j}(z) \cdot E_{bj}. \quad (6)$$

$\varepsilon_{x,j}^m(z)$ ,  $\varepsilon_{x,j}^{\text{res}}$  and  $\varepsilon_{x,j}(z)$  denote the mechanical strain, the eigenstrain and the total strain, respectively of the  $j$ -th layer.  $E_{bj}$  is the biaxial Young's modulus of each sublayer calculated from the Young's modulus  $E_j$  and Poisson's ratio  $\nu_j$  as,

$$E_{bj} = \frac{E_j}{1-\nu_j}. \quad (7)$$

Assuming that there is no material separation during deformation, the strain distribution over the cantilever thickness has to be linear following Eq. (8),

$$\varepsilon_{x,i}(z) = \kappa_i z + d_i, \quad (8)$$

where  $\kappa_i$  denotes the actual curvature determined with Eq. (3) and  $d_i$  is the offset strain at the zero  $z$  position. Note, that  $\kappa_i$  can only be

determined referring to the neutral axis. By definition Eq. (3) refers to the neutral axis therefore the  $z$ -coordinate must be offset.

This results in a system of equations with two unknowns,  $\sigma^{\text{res}}$  and  $d_i$ , that must be solved for each sublayer.

In the following, the calculation procedure is explained in detail and summarized in Fig. 2a–e.

The calculation starts with the uncoated substrate denoted as “condition zero”. The substrate consists of pure single crystalline silicon, is stress free and therefore undeformed and plane, see Fig. 2a, corresponding to the curvature  $\kappa_0 = 0$  and the uniform stress distribution  $\sigma_{x,0}(z) = 0$ .

In the next step the first sublayer of thickness  $t_{\text{sublayer } 1}$  is attached onto the silicon substrate (Fig. 2b). In the present example sublayer 1 consists of TiN with a thickness of 120 nm and contains eigenstress. The eigenstress is a result of the lattice mismatch of substrate and layer, so it corresponds to the stress necessary to shrink or extend the layer to match the lattice of the substrate. Introducing eigenstress in the system leads to a bending of the substrate and sublayer 1 (Fig. 2c). Due to the attachment of sublayer 1, the force and moment balance as well as the position of the neutral axis change. The uniform eigenstress in the sublayer is now calculated by solving Eqs. (4) and (5).

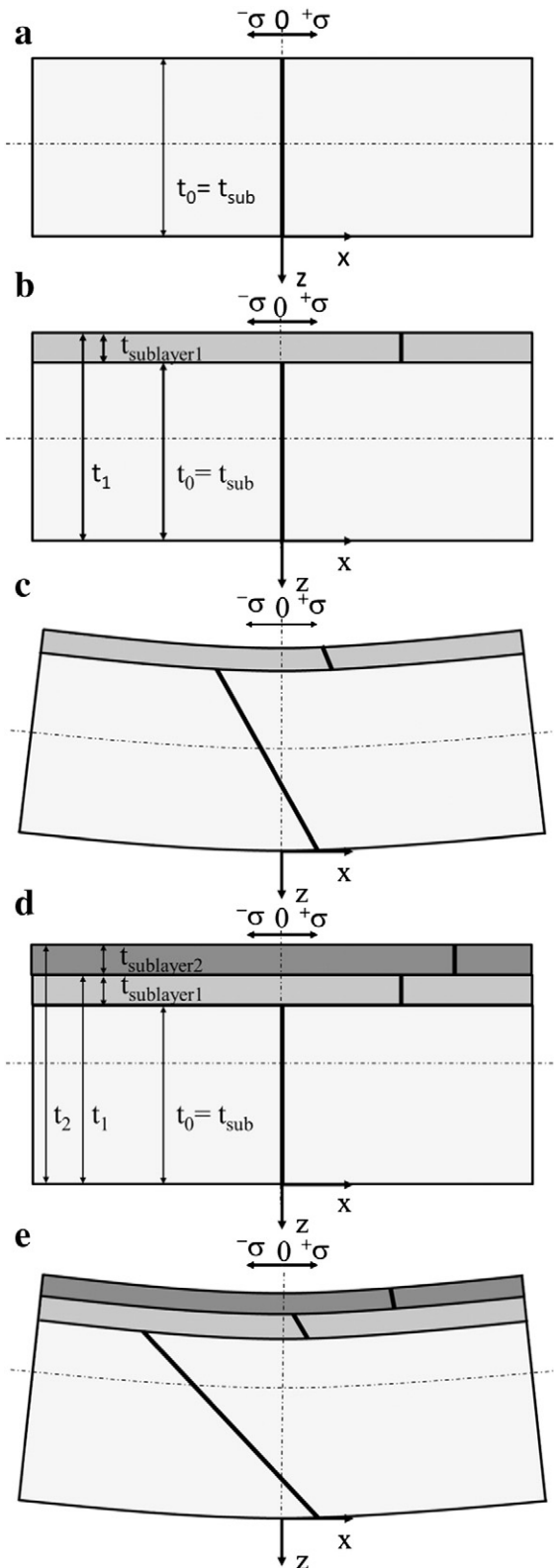


**Fig. 2.** Schematic description of the calculation procedure. a) Undeformed and stress free substrate, b) undeformed and stress free substrate plus undeformed sublayer 1 with constant eigenstress  $\sigma_1^{\text{res}}$ , c) relaxed system (substrate and sublayer 1) with total stress distribution over height, d) undeformed and stress free substrate plus undeformed sublayer 1 with constant eigenstress  $\sigma_1^{\text{res}}$  and undeformed sublayer 2 with constant eigenstress  $\sigma_2^{\text{res}}$ , e) relaxed system (substrate and sublayers 1 and 2) with total stress distribution over height.

In the following steps sublayer by sublayer is attached on top of the previously calculated system (Fig. 2d–e), each one containing its specific eigenstress. The curvature that corresponds to the thickness of the actual relaxed system  $\kappa_{Ai}$  is calculated from Eq. (3). From these curvatures, stresses can be readily obtained.

### 3. Experiments

In order to investigate the influence of manufacturing related variations in the cantilever geometry as well as the influence of the boundary conditions, the stress distribution in a real film system, consisting of a W and TiN film on a Si substrate, is determined. The investigated sample has an approx. 800 nm thick W layer and a 120 nm thick TiN interlayer, which works as primer, deposited on a single crystalline Si substrate (wafer) with a (100) orientation. The diameter and the thickness of the wafer are 200 mm and approx. 700  $\mu\text{m}$ , respectively. For the Young's modulus and Poisson's ratio of Si mean values from different values reported in the literature [30–33] are used, indicating a Young's modulus and Poisson's ratio of 170 GPa and 0.28, respectively. The TiN as well as the W film were deposited via chemical vapor deposition (CVD). Depending on the deposition technique the elastic properties of TiN and W films may vary, and the reported scatter of Young's modulus and Poisson's ratio is given in Table 1 [34–42]. Especially TiN films show a very large scatter in elastic properties [34–39]. In the present case the Young's modulus and Poisson's ratio for TiN were taken as 390 GPa and 0.34, respectively. Thin W films behave more like bulk materials and the scatter of elastic properties is low [40–42]. The values chosen for the Young's modulus and Poisson's ratio of W were 411 GPa and 0.28, respectively. In the present case all materials are assumed to be homogeneous and isotropic without any texture. This assumption has been made because no pronounced texture in the W film was observed by using XRD. Furthermore, only negligible deviation in the numerical determined stress profile were determined if the assumed isotropic elastic behavior of the single crystalline Si substrate was substituted by an orthotropic elastic behavior. However this assumption is a critical point that has to be considered for every system of interest before applying the analytical approach.

#### 3.1. Sample preparation

Micro-scaled cantilevers are prepared to determine the local residual stress distribution in the thin film system. Two different ion milling techniques are employed to manufacture these cantilevers. As FIB milling is rather expensive and time-consuming, broad beam ion milling is employed – a technique which was used by Wurster et al. [43] to manufacture freestanding lamellae.

The sample is retrieved from the middle of the wafer to avoid any influence on the stress distribution by inhomogeneous deposition near the wafer edge. First the ion slicing technique is used to mill a narrow fillet. Here, low energy Ar ions polish the surface, leading to less ion damage in the thinned area than the FIB. A Hitachi-E3500 Cross Section Polisher (Hitachi, Japan) is utilized for this preparation step. Fig. 3a shows a schematic of the sample setup that is put into the ion slicer. Every material that is not covered by the mask is exposed to the ion beam and therefore removed. A lacquer covering the sample surface protects the sensitive metal film from ion damage. In the first milling step the front edge of the sample is polished. A layer with a thickness of about 80–100  $\mu\text{m}$  is removed to exclude possibly deformed material

**Table 1**

Range of elastic properties of single crystalline Si (100) [30–33], TiN [34–39] and W [40–42].

$E_{\text{Si}} \langle 1 \ 1 \ 0 \rangle$ [GPa]	$E_{\text{TiN}}$ [GPa]	$E_{\text{W}}$ [GPa]
160–180	150–400	380–420
$\nu_{\text{Si}} \langle 1 \ 1 \ 0 \rangle$	$\nu_{\text{TiN}}$	$\nu_{\text{W}}$
0.28–0.34	0.28–0.34	0.28–0.3

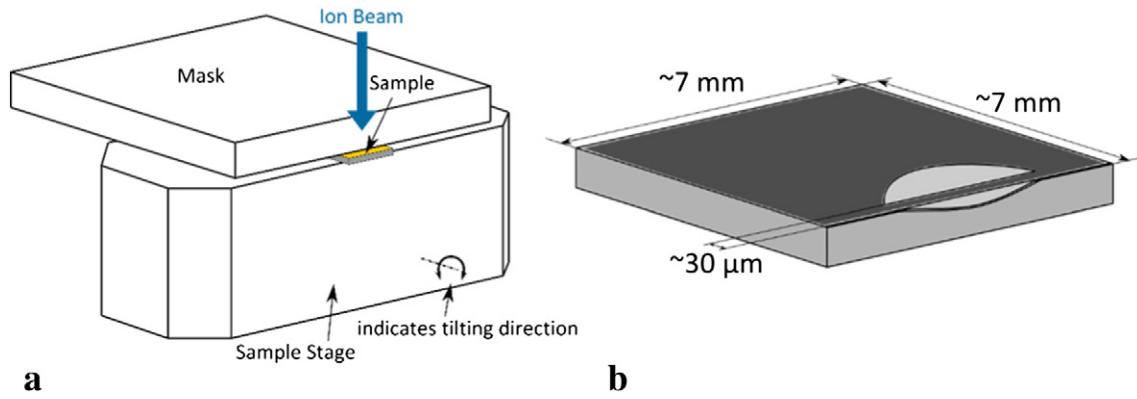


**Fig. 3.** a) Schematic of the sample setup that is put into the ion slicer. b) Schematic of a sample after ion milling, showing the fillet of  $\sim 30 \mu\text{m}$  metal film (dark gray) on Si substrate (gray).

which results from breaking the wafer. After rotating the sample by  $180^\circ$  a narrow area is covered by the mask so that a fillet on the Si substrate of about  $20\text{--}30 \mu\text{m}$  metal film remains (Fig. 3). For each milling step the ion beam is switched on for 3 h with an acceleration voltage of 6 kV, a discharge voltage of 4 kV and a sample tilting angle of  $\pm 25^\circ$  with a speed of 1 rpm. The tilting of the sample with respect to the ion beam results in a more homogeneous material removal.

For the second preparation step the sample is loaded in a LEO 1540XB (Zeiss, Germany) FIB workstation to shape the final cantilevers (Fig. 1a). The coarse shape is milled with an ion beam current of 10 nA, and the final polishing step is carried out with 500 pA to minimize  $\text{Ga}^+$  ion damage [29]. For details concerning the FIB preparation procedure see Massl et al. [23]. The final cantilever has a length of approx.  $100 \mu\text{m}$  and a cross-section of approx.  $5 \times 4 \mu\text{m}^2$ . For the actual experiment the cantilever is first cut free on one side and then gradually thinned in an approx.  $10 \mu\text{m}$  wide ILR area (Fig. 1a; blue solid rectangle) with a FIB cutting current of 500 pA to determine the deflections as a function of the remaining cantilever thickness. The used SEM imaging parameters were: In-lens detector, 10 kV acceleration voltage,  $30 \mu\text{m}$  objective aperture, scan speed 9 and noise reduction rate 4. Each sublayer thickness is determined from the difference between initial and remaining cantilever thickness in the ILR area. To minimize systematic errors in the SEM-measured dimensions, such as length, height, cutting depth or deflection, it is essential to calibrate the SEM well. Using a calibrated SEM leads to a standard deviation of all SEM-measured dimensions of less than 20 nm. To exclude any possible influence of the e-gun drift, we compare images with a scan rotation of  $0^\circ$  and  $90^\circ$  by considering beam deflection. The difference based on the deflection measurements between the two rotations is approx. 1%, and found in the sub-pixel regime using absolute numbers. The calculated drift is then even less than the measurement accuracy. Therefore, we conclude that the influence of the e-gun drift has no significant impact on the determined stress distribution. The measured deflections and sublayer thicknesses for this experiment are given in Table 2. The change of the cantilever deflection during FIB milling has two main reasons. The first reason is due to the fact that the internal loading change, since a part of the material which contains residual stresses is cut away. The second reason causing a change of the cantilever deflection is, that the moment

of inertia changes during FIB milling. Therefore, an increasing deflection during layer removal is not directly related to compressive stresses in the removed layer. If the change of the moment of inertia is higher than the decrease in the loading, the deflection can increase although tensile residual stresses are present in the sublayer. The measured deflections are consequently used to determine the curvature of the ILR area using Eqs. (2) and (3), see Section 2. The resulting curvatures are given in Table 2.

### 3.2. Stress determination by means of X-ray diffraction

In order to obtain an integral measure of the mean residual stresses present in the W film and to validate the ILR method, X-ray diffraction (XRD) measurements are carried out. All experiments are conducted on a D8 Discover diffractometer (Bruker AXS, Germany) in parallel beam geometry at 40 kV and 35 mA using  $\text{Cr K}\alpha$  radiation. The dimensions of the investigated samples are approx.  $10 \times 10 \times 0.7 \text{ mm}^3$ . For the residual stress determination in the W film the conventional  $\sin^2\psi$  technique [1,10] was used. X-ray diffraction enables only the determination of a volume average of the residual stress. Therefore, the obtained residual stress value of  $1433 \pm 47 \text{ MPa}$  found in the W film (without TiN), represents a mean value which depends on the actual residual stress profile, the X-ray penetration depth and the geometry of the experiment. The mean penetration depth up to 62.5% absorption of the primary beam for  $\text{Cr K}\alpha$  radiation in the W film is approx. 500 nm. Consequently the main information for the average residual stress originates from the first 500 nm of the W film.

## 4. Numerical determination of the residual stress distribution

A detailed three dimensional (3D) FE model closely matching the experimental situation is created with the FE software package ABAQUS [44] and coupled with an optimization program.

The residual stress distribution in the numerical model is adjusted by means of a conventional least-squares algorithm until the deflection of the cantilever in the model matches the experimentally measured values. The following section deals with the detailed description of the FE model and the used optimization strategy.

The dimensions of the cantilever (length, width, height, length of ILR area, thickness of layers and sublayers) as well as the deflection (measured at the tip of the cantilever) are taken from the experiments explained above, see Fig. 1a–e. At first a FE model using the same assumptions as used in the analytical calculation (idealized geometry and rigid fixation) is created (Fig. 4a–b) in order to compare the analytical and numerical results and to estimate the accuracy of the numerically determined stress profile. To model a rigid fixation all nodes on the left side of the cantilever are fixed in all directions, see Fig. 4a–b. Afterwards the FE model is changed by adding an elastic fixation, see Fig. 4c–d. This is closer to the situation in the experiment. Finally

**Table 2**  
Measured cutting depths and deflections during gradual film reduction. Cantilever curvatures calculated from the measured deflections using Eqs. (2) and (3).

Sublayer thickness [ $\mu\text{m}$ ]	Deflection [ $\mu\text{m}$ ]	Curvature [ $1/\text{mm}$ ]
0	$3.815 \pm 0.015$	$0.93809 \pm 3.69 \cdot 10^{-3}$
$0.135 \pm 0.015$	$3.914 \pm 0.012$	$1.06244 \pm 3.89 \cdot 10^{-3}$
$0.105 \pm 0.015$	$3.972 \pm 0.017$	$1.13366 \pm 6.18 \cdot 10^{-3}$
$0.078 \pm 0.014$	$3.960 \pm 0.017$	$1.11892 \pm 6.18 \cdot 10^{-3}$
$0.248 \pm 0.015$	$3.605 \pm 0.010$	$0.68307 \pm 2.42 \cdot 10^{-3}$
$0.191 \pm 0.014$	$3.102 \pm 0.014$	$0.00656 \pm 2.49 \cdot 10^{-4}$

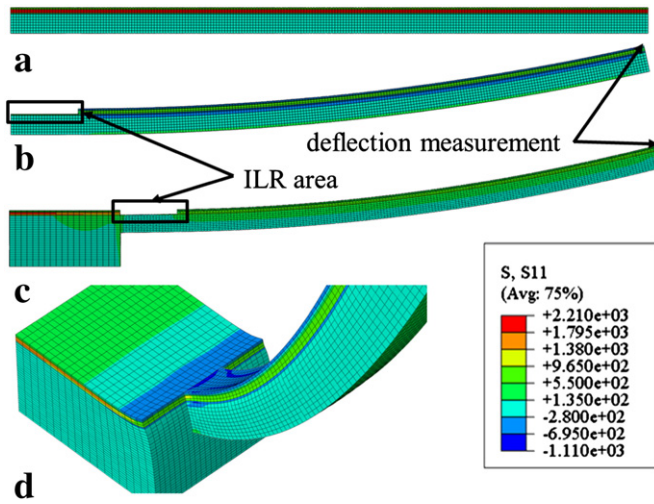


**Fig. 4.** In-plane stress distribution  $S_{11}$  in the cantilever with a rigid fixation (a and b) and an elastic fixation (c and d). The upper limit (red color) is set to 2210 MPa. The lower limit (blue color) is set to  $-1110$  MPa. a) Initial stress distribution in the undeformed cantilever with a rigid fixation. b) Stress distribution and shape after film removal in the ILR area (black rectangle) for a cantilever with a rigid fixation. c) Stress distribution and shape for a cantilever with an elastic fixation (tied to an elastic “box”) after film removal in the ILR area (black rectangle). The deflection is measured for every calculation step at the tip of the cantilever. d) Detailed view of the fixation region with a deformation scale factor of 80. The fixation is notably elastically deformed.

different FE models with a slightly changed cantilever geometry and position of the ILR area are created to study the manufacturing related variations.

To determine the residual stresses in the sublayers different calculation steps are introduced in all above indicated models. In the initial step an arbitrary residual stress distribution is applied as predefined field variable in the initial step in order to load the cantilever. The arbitrary residual stress distribution leads to a perturbation of the equilibrium which is restored by stress relaxation in the first calculation step, leading to a deflection of the cantilever.

The direction and magnitude of the deflection depends on the arbitrarily chosen residual stress distribution. In subsequent steps, the FIB milling in the ILR area is modeled by deleting element rows (Fig. 4b and Fig. 4c), leading to a change of the deflection line of the cantilever.

A special modeling technique called “model change” [44] allows setting the stiffness of selected elements to almost zero.

In order to save calculation time, each sublayer is modeled with only one element over height. The element length and width is chosen in a way that the element aspect ratio (height : length or width) does not exceed 1:6. To minimize the numerical error during the deflection calculation, fully integrated second order hexagonal brick elements are used.

The deflection in each calculation step is determined from the displacement of one node at the cantilever tip (see Fig. 4b–c) and subsequently compared with the experimentally determined deflection. Afterwards, a least squares optimization algorithm (Levenberg–Marquardt algorithm [45,46]) is used to minimize the deviation between simulated and experimentally measured deflections.

The Levenberg–Marquardt algorithm is an iterative procedure, like many other numerical minimization algorithms. To start a minimization, an initial guess for the stress distribution in the layer system (parameter vector) has to be made. The optimization loop stops if the reduction of the sum of the squares from the preceding parameter vector falls below predefined limits. The last parameter vector is then considered to be the solution.

## 5. Results and discussion

The analytically and numerically determined stress distribution in the W and TiN film is shown in Fig. 5a, where the black solid line represents the analytical result and the red dashed line shows the FE result. The analytical as well as the numerical results show a large stress gradient inside the W film. Starting from  $238 \pm 15$  MPa in the TiN interlayer, the stress increases rapidly in the W film and reaches a maximum value of  $2300 \pm 56$  MPa at a depth of approx. 400 nm from the surface, as calculated analytically. After reaching the maximum, the stresses decrease toward the surface and reach a value of  $633 \pm 21$  MPa in the top sublayer of the W film. The scatter of the so-determined stresses is relatively low since only the inaccuracies of the SEM measurements enter the calculations.

A comparison of the stress distributions derived from the two approaches (Fig. 5a) indicates a good agreement, only the stress value in the TiN interlayer shows a significant discrepancy in the residual stress ( $238 \pm 15$  MPa analytically and  $456 \pm 18$  MPa numerically determined). However the measured and the calculated deflections of the

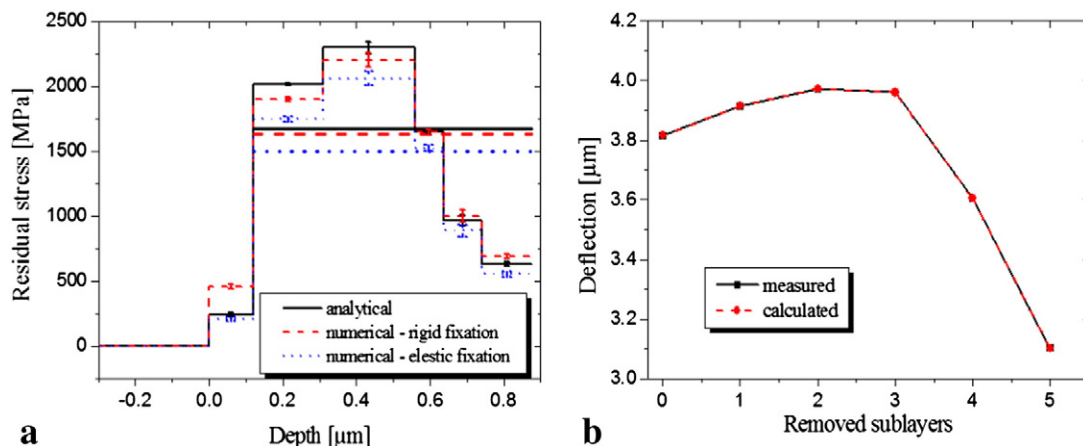


**Fig. 5.** a) Stress distribution in the film system determined analytically (black solid line) and numerically with a rigid fixation (red dashed line) and with an elastic fixation (blue dotted line). Additionally, three mean stresses are plotted, corresponding to the weighted average of the analytically determined stresses working in the W film (black solid line), the weighted average of the numerically determined stresses (red dashed line) using a rigid fixation and the weighted average of the numerically determined stresses (blue dotted line) using a rigid fixation. The error bars represent the scatter in the stress values with respect to the measurement inaccuracies. b) Measured (black solid line) and calculated (red dashed line) deflection of the cantilever as a function of removed sublayers. The difference is less than  $10^{-4}$   $\mu\text{m}$ .

cantilever are in an excellent agreement (see Fig. 5b), i.e., the difference is nowhere greater than  $10^{-4}$   $\mu\text{m}$ .

Additionally, the mean stress values calculated from the sublayer values as a weighted average over all W sublayers,

$$\bar{\sigma} = \frac{\sum_{i=1}^n \sigma_i^{\text{res}} \cdot t_i}{\sum_{i=1}^n t_i} \quad (9)$$

are plotted in Fig. 5a.  $t_i$  denotes the sublayer thickness. In the mean stress calculation the residual stresses working in the TiN interlayer are not taken into account. The black solid line represents the mean stress calculated from the analytically determined stresses and is  $1680 \pm 23$  MPa. The red dashed line shows the mean stress calculated from the numerically determined stresses and is  $1634 \pm 21$  MPa. The values are in an excellent agreement. In comparison with the XRD measured residual stress, which is  $1433 \pm 47$  MPa in the W film, the values are reasonable. The calculated residual stress in the W film is approx. 15% higher than in the corresponding XRD measurement. The difference can be attributed to the mean penetration depth of only  $\sim 500$  nm. The stress magnitudes at positions below this depth are overemphasized due to the exponential absorption of X-rays in solids according to Lambert–Beer's law [1,10].

### 5.1. Influence of boundary conditions, geometry and cantilever fabrication

In Massl et al. [23–25] it has been shown that FIB damage as well as plastic deformation, cracking and stress redistribution during gradual FIB milling has no pronounced influence on the stress distribution in the film as long as the deformation of the cantilever is not too large. In [25], Massl et al., propose guidelines for the correct geometry and the experimental procedure. Following these guidelines, the systematical and statistical errors can be minimized. In this paper, we will take a step further and investigate the influence of the geometry and different boundary conditions as well as the stress rearrangement during cantilever fabrication.

#### 5.1.1. Influence of elastic fixation

Both, the analytical as well as the numerical results, assume a rigid fixation of the cantilever. However, in reality the cantilever is connected elastically with the remaining wafer. To consider the elastic fixation, a FE calculation including a part of the remaining wafer was performed. Fig. 4c–d shows the 3D FE model of the cantilever consisting of the layer system, the substrate and a representative part of the wafer in the following referred to as “box”. The size of the box is chosen such that a further increase of the box size has no influence on the results. In order to reproduce the behavior of a large wafer, all degrees of freedom of the nodes on the surface, except the top surface and the right side of the box, are fixed. The residual stress distribution is determined in analogy to the approach explained in Section 4, only the FE model is changed as outlined above. Fig. 4d shows a detailed view of the fixation region with a deformation scale factor of 80. It can be clearly seen that the “box” in the vicinity of the fixation is elastically deformed. Therefore, an elastic fixation of the cantilever results in a reduction of the stresses over the entire layer thickness, as the cantilever can bend more freely in comparison to the rigid fixation. Fig. 5a shows the residual stress profiles for the rigid (red dashed line) and the elastic fixation (blue dotted line). Additionally, the analytical solution (black solid line) and the mean stress calculated from the sublayer values are shown in Fig. 5a. The stress reduction is almost constant across all sublayers in the W film and amounts to approx. 150 MPa, which is about 9% of the mean residual stress in the W film ( $\bar{\sigma} = 1634 \pm 21$  MPa). The stress reduction in the TiN interlayer is 250 MPa with leads to a residual stress of 206 MPa. Therefore, the influence of an elastic fixation on the determined residual stresses in the W film as well as in the TiN interlayer is significant and shall be considered.

#### 5.1.2. Influence of geometry

The geometry of the cantilever will influence the stress profile as well. Not only the dimensions of the cantilever, which are included in the analytical description, but also the position of the ILR area and the geometry of the transition between cantilever and wafer will have an influence on the stress profile. During FIB preparation a sharp transition between the cantilever and the wafer cannot be realized. To study this effect, a FE model with a smooth transition radius of 1  $\mu\text{m}$  at the bottom of the cantilever, in the following denoted as case A, has been created, see Fig. 6a. Furthermore, two models with an alternative position of the ILR area, denoted as case B and case C, are created to study the influence of varying positions of the ILR area, see Fig. 6b and Fig. 6c. In case B (Fig. 6b) the ILR area is shifted by 4  $\mu\text{m}$  toward the fixed end into the wafer, in case C the ILR area is shifted by 4  $\mu\text{m}$  in the opposite direction toward the free end of the cantilever. The stress distribution which is found for the model with elastic fixation is prescribed as predefined field in all three cases in order to deform the cantilever.

During the following calculation steps, the stresses in the sublayers relax and lead to a deflection of the cantilever. In this case the focus is on the validation of the deflection; hence no residual stress analysis is performed. The calculated displacements, measured at the cantilever tip, are shown in Fig. 6d. The black solid line shows the calculated deflection of the cantilever as a function of removed sublayers for the reference geometry (cantilever with “box” and sharp transition). The red dashed line shows the calculated deflection for case A. The displacements of the cantilever tip are in all steps lower than for the reference geometry. The radius in the transition region leads to an increased stiffness of the system, which lowers the deflection of the cantilever if the same residual stress distribution is initially present in the film system. Thus, to reach the same experimental displacement an increased residual stress distribution is necessary. However, the differences in deflection are less than 1.5% leading to only a slightly changed residual stress profile. The blue dotted and magenta dash-dotted lines (Fig. 6d) show the displacements for case B and C. It can be seen that a shift of the ILR area, which is in this simulation exaggerated compared to experimental inaccuracies, influences the displacements only slightly; the change is less than 1% in almost all points. Therefore, the influence of a misplaced ILR area as well as the influence of a rounded transition on the stress profile are low and can be neglected in the residual stress determination.

#### 5.1.3. Influence of cantilever fabrication

Since the residual stress distribution in the film system deposited on the wafer is of interest, the question arises whether the changed stiffness of the system due to fabrication of the cantilever influences the residual stress state in the film system or not. Stefanelli et al. [47] showed that the sample preparation can have a large influence on the stress situation in the film, in particular when large parts of the material are removed during sample preparation. In order to investigate the influence of cantilever fabrication, FE studies are carried out. The wafer is modeled as block where the dimensions of the block ( $0.6 \times 0.3 \times 0.15$  mm<sup>3</sup>) are chosen such that the boundaries do not influence the area of interest. Furthermore, the block is fixed to suppress free body movement and rotation. Only half of the block is modeled and symmetric boundary conditions are applied at the symmetry plane. Again fully integrated second order brick elements are used. Two calculation steps are performed. In the first step the residual stresses, prescribed as initial condition, relax and the wafer bends slightly in order to bring the structure into its mechanical equilibrium. In the second step the cantilever fabrication is simulated by means of a model change technique [44]. To quantify the effect of the cantilever fabrication, in the FE calculation again a Levenberg–Marquardt optimization is carried out, where the residual stresses in the film system are iteratively adjusted until the relaxed residual stress after cantilever fabrication matches the stresses obtained from the ILR experiment. Since the stress profile using an elastic fixation is the most realistic solution, these stresses are used as target

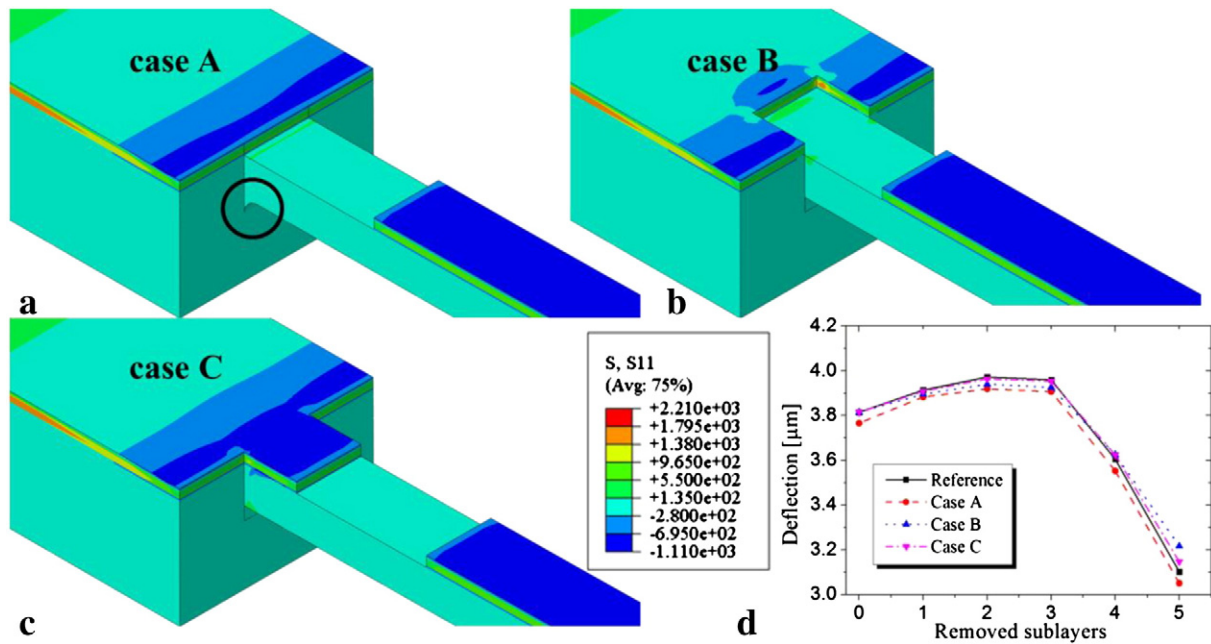


**Fig. 6.** 3D in-plane stress distribution (S11) in the cantilever and in the vicinity of the ILR area (“box”) for different geometries: a) Case A (rounded transition between cantilever and box). The position of rounded transition is highlighted with a black cycle. b) Case B: ILR area is shifted toward the remaining wafer. c) Case C: ILR area is shifted toward the cantilever tip. d.) Calculated deflection of the cantilever as a function of removed sublayers for the reference geometry (black solid line), case A (red dashed line), case B (blue dotted line) and case C (magenta dash-dotted line).

values for the optimization. Fig. 7a shows a detailed view of the in-plane stress distribution (S11) in the cantilever and in the wafer after cantilever fabrication. The upper limit (red color) is set to 2210 MPa and the lower limit (blue color) to  $-1110$  MPa. The black solid rectangle indicates the position at which the residual stress profile (violet dash-dotted line in Fig. 7b) was determined in the unaffected wafer. The red dashed rectangular indicates the position at which the residual stress profile (blue dotted line in Fig. 7b) in the cantilever was determined. Additionally the analytically determined stress profile is plotted (black solid line) in Fig. 7b.

It can be seen that there is a significant stress relief during cantilever fabrication. The stress reduction is between 160 MPa in the TiN

interlayer and 270 MPa at the maximum stress in the W film. Additionally, three mean values are plotted, corresponding to the weighted average of the residual stresses working in the unaffected W film on the wafer,  $\bar{\sigma} = 1774$  MPa (violet dash-dotted line), the weighted average of the residual stresses working in the W film on the cantilever,  $\bar{\sigma} = 1482$  MPa (blue dotted line) and the measured stresses in the W film on the wafer, and  $\sigma = 1433$  MPa (black dashed line) obtained by XRD. The mean value of the stresses in the unaffected wafer is approx. 290 MPa higher than those of the stresses in the cantilever, which is significant and should be considered in the residual stress determination. In comparison with the stresses obtained from XRD measurements the calculated mean stress in the unaffected wafer is approx. 340 MPa

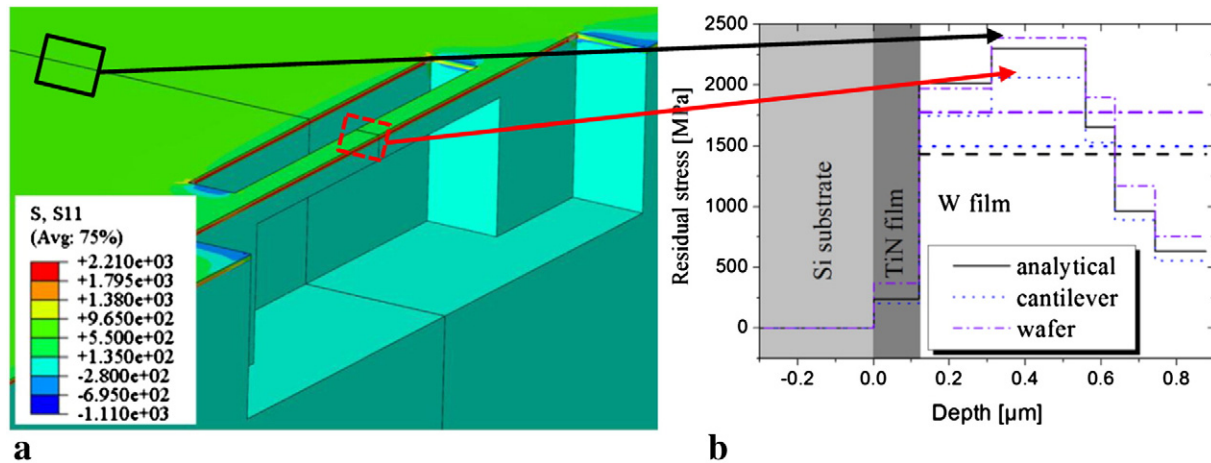


**Fig. 7.** Stress distribution in the cantilever and wafer after cantilever fabrication. a) Detailed view of the 3D in-plane stress distribution (S11) at the cantilever and in the vicinity of the cantilever. The upper and lower limits are set to 2210 MPa (red color) and  $-1110$  MPa (blue color), respectively. The black solid rectangle indicates the position at which the residual stresses were determined in the unaffected wafer. The red dashed rectangle indicates the position at which the residual stresses in the cantilever were determined. b) Residual stress distribution in the film system determined in the middle of the cantilever (red dashed rectangle) and in the unaffected wafer (black solid rectangle). Additionally, three mean values are plotted, corresponding to the weighted average of the residual stresses working in the unaffected wafer (violet dash-dotted line), the weighted average of the residual stresses working in the cantilever (blue dotted line) and the measured stress in the wafer (black dashed line) obtained by XRD.

higher. However, the difference between the calculated mean stress in the unaffected wafer and the residual stress obtained from XRD measurements can be explained by the exponential absorption of X-rays in solids according to Lambert–Beer's law, as outlined above.

#### 5.1.4. Remarks on the elastic properties of the materials involved

The stress profile in the film system is calculated from the strains in the system and therefore depends on the elastic properties of the materials involved. As mentioned in Section 3, the elastic properties of thin films are strongly influenced by the deposition technique and their measurement is challenging. In principle, different measurement techniques are available [48–53], but they are not generally suited to determine the elastic properties of films at the nano-scale. To get an impression on how the elastic properties can affect the stress distribution, the upper and lower values for the material properties found in the literature [30–42] are used to determine a bandwidth of the stress profile. To quantitatively show the influence of the uncertainties of the elastic properties, other sources of scatter, e.g. inaccuracies of the SEM measurements and other geometric aspects, are not taken into account. Furthermore, the stresses are determined using the analytical approach. Fig. 8 shows the stress distribution calculated with the minimum values (black solid line) and the maximum values (red dashed line) of the Young's moduli and Poisson's ratios, taken from Table 1. Additionally, the weighted mean values are shown. The shape of the stress profile remains unaffected, but the mean value is shifted in the range from 1564 MPa to 1778 MPa. Notably, the stress value in the TiN interlayer does not scatter very strongly (approx. 30%) even though the moduli differ by more than 150%. Furthermore, it can be shown that the values as well as the stress profile in the W film are only slightly influenced by the stress values of the interlayer. Thus, the interlayer properties have only a small influence on the determined stress distribution in the W film.

## 6. Conclusions

The ILR method was applied to determine the stress profile in an 800 nm thick W film with a 120 nm TiN interlayer deposited on a single crystalline silicon wafer. Two methods are used to determine the stresses from the deflection of the cantilever. The first is an analytical approach based on the Euler–Bernoulli beam theory. The second approach uses a least squares optimization coupled with a finite element simulation of the experiment. It is shown that the analytically determined stress distribution is in good agreement with the numerically determined one.

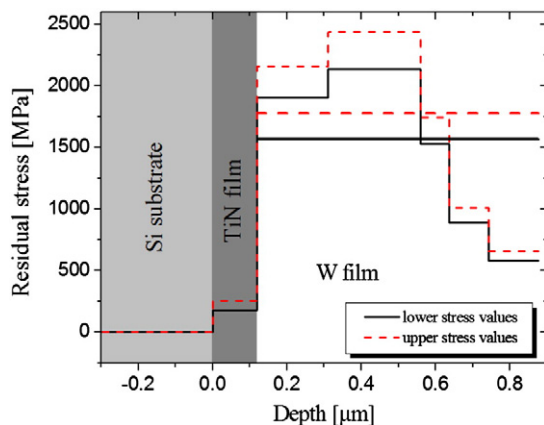


**Fig. 8.** Stress distribution in the film system determined analytically using different elastic properties. The red dashed line shows the stress distribution calculated with maximum values, while the black solid line uses minimum values. Additionally, the mean value (red dash-dot line) for the upper stress limit and the mean value (black solid line) for the lower stress limit is plotted.

Numerical case studies investigating the influence of fixation, cantilever geometry and cantilever fabrication are performed. They show a slight influence of the cantilever geometry, such as the radius in the fixation region or a shifted ILR area, on the deflections of the cantilever and therefore also a small influence on the stress distribution.

Additionally, we show that a realistic elastic fixation instead of the previously considered rigid one results in higher deflections at the cantilever tip. Consequently, to reach the measured deflections, lower stresses in the film system are necessary. We demonstrate that the influence of fixation is pronounced and cannot be neglected for stress determination.

Moreover, the influence of the cantilever fabrication on residual stress relief is investigated. The cantilever fabrication leads to a significant stress relief, so that the residual stresses determined with the ILR method underestimate the stress situation in the initial wafer which has to be accounted for.

Once realistic low dimensional structures such as conductivity lines or through silicon vias are considered rather than flat model systems, very comparable relaxations mechanisms act on the real structure, which can now be adequately considered as shown in this work.

## Acknowledgment

The authors thank H.P. Gänser, P. Angerer, H.P. Krückl and A. Drlicek for their helpful discussions and support. Furthermore, we thank E. Schirgi and R. Niedermeyer from Austria Microsystems (AMS) for providing the samples. Financial support by the Austrian Federal Government (837900) (in particular from the Bundesministerium für Verkehr, Innovation und Technologie and the Bundesministerium für Wirtschaft, Familie und Jugend) represented by Österreichische Forschungsförderungsgesellschaft mbH and the Styrian and the Tyrolean Provincial Government, represented by Steirische Wirtschaftsförderungsgesellschaft mbH and Standortagentur Tirol, within the framework of the COMET Funding Programme is gratefully acknowledged. In addition partly financial support has been given by the FFG project 838841.

## References

- [1] V. Hauk, *Structural and Residual Stress Analysis by Nondestructive Methods*, Elsevier, 1997.
- [2] S. Chen, T.V. Baughn, Z.J. Yao, C.L. Goldsmith, A new in situ residual stress measurement method for a MEMS thin fixed–fixed beam structure, *J. Microelectromech. Syst.* 11 (2002) 309.
- [3] V. Sarihan, Role of film intrinsic stress in packaging of multi-layer microelectronic structures, *Mater. Sci. Eng. A* 421 (2006) 109.
- [4] M. Sebastiani, E. Bemporad, G. Melone, L. Rizzi, A.M. Korsunsky, *AIP Conference Proceedings*, vol. 1300, 2010, p. 120.
- [5] L.A. Starman Jr., E.M. Ochoa, J.A. Lott, M.S. Amer, W.D. Cowan, J.D. Busbee, Residual stress characterization in MEMS microbridges using micro-Raman spectroscopy, 2002 International Conference on Modeling and Simulation of Microsystems – MSM 2002, 2002, p. 314.
- [6] G.G. Stoney, The tension of metallic films deposited by electrolysis, *Proc. R. Soc. London, Ser. A* 82 (553) (1909) 172.
- [7] L.B. Freund, S. Suresh, *Thin Film Materials: Stress, Defect Formation and Surface Evolution*, Cambridge University Press, Cambridge, U.K., 2003.
- [8] P.J. Withers, H.K.D.H. Bhadeshia, Residual stress part 2 – nature and origins, *Mater. Sci. Technol.* 17 (2001) 366.
- [9] J.-S. Chung, G.E. Ice, Automated indexing for texture and strain measurement with broad-bandpass X-ray microbeams, *J. Appl. Phys.* 86 (1999) 5249.
- [10] I.C. Noyan, J.B. Cohen, *Residual Stress: Measurement by Diffraction and Interpretation*, Springer, New York, 1987.
- [11] E. Eiper, K.J. Martinschitz, J. Keckes, Combined elastic strain and macroscopic stress characterization in polycrystalline Cu thin films, *Powder Diffr.* 21 (2006) 25.
- [12] J. Keckes, M. Bartosik, R. Daniel, C. Mitterer, G. Maier, W. Ecker, J. Vila-Comamala, C. David, S. Schoeder, M. Burghammer, X-ray nanodiffraction reveals strain and microstructure evolution in nanocrystalline thin films, *Scr. Mater.* 67 (2012) 748.
- [13] M. Bartosik, R. Daniel, C. Mitterer, I. Matko, M. Burghammer, P.H. Mayrhofer, J. Keckes, Cross-sectional X-ray nanobeam diffraction analysis of a compositionally graded CrN thin film, *Thin Solid Films* 542 (2013) 1.
- [14] K. Sasaki, M. Kishida, T. Itoh, The accuracy of residual stress measurement by the hole-drilling method, *Exp. Mech.* 37 (1997) 250.

- [15] K.J. Kang, N. Yao, M.Y. He, A.G. Evans, A method for in situ measurement of the residual stress in thin films by using the focused ion beam, *Thin Solid Films* 443 (2003) 71.
- [16] N. Sabaté, D. Vogel, A. Gollhardt, J. Marcos, I. Gràcia, C. Cané, B. Michel, Digital image correlation of nanoscale deformation fields for local stress measurement in thin films, *Nanotechnology* 17 (2006) 5264.
- [17] N. Sabaté, D. Vogel, A. Gollhardt, J. Keller, C. Cané, I. Gràcia, J.R. Morante, B. Michel, Residual stress measurement on a MEMS structure with high-spatial resolution, *J. Microelectromech. Syst.* 16 (2007) 365.
- [18] B. Winiarski, P.J. Withers, Mapping residual stress profiles at the micron scale using FIB micro-hole drilling, *App. Mech. Mater.* 24–25 (2010) 267.
- [19] A.M. Korsunsky, M. Sebastiani, E. Bemporad, Focused ion beam ring drilling for residual stress evaluation, *Mater. Lett.* 63 (2009) 1961.
- [20] M. Krottenthaler, C. Schmid, J. Schaufler, K. Durst, M. Göken, A simple method for residual stress measurements in thin films by means of focused ion beam milling and digital image correlation, *Surf. Coat. Technol.* 215 (2013) 247.
- [21] A.M. Korsunsky, M. Sebastiani, E. Bemporad, Residual stress evaluation at the micrometer scale: analysis of thin coatings by FIB milling and digital image correlation, *Surf. Coat. Technol.* 205 (2010) 2393.
- [22] M.D. Uchic, D.M. Dimiduk, J.N. Florando, W.D. Nix, Sample dimensions influence strength and crystal plasticity, *Science* 305 (2004) 986.
- [23] S. Massl, J. Keckes, R. Pippan, A direct method of determining complex depth profiles of residual stresses in thin films on a nanoscale, *Acta Mater.* 55 (2007) 4835.
- [24] S. Massl, J. Keckes, R. Pippan, A new cantilever technique reveals spatial distributions of residual stresses in near-surface structure, *Scr. Mater.* 59 (2008) 503.
- [25] S. Massl, H. Köstenbauer, J. Keckes, R. Pippan, Stress measurement in thin films with the ion beam layer removal method: influence of experimental errors and parameters, *Thin Solid Films* 516 (2008) 8655.
- [26] L.M. Jiang, J. Peng, Y.G. Liao, Y.C. Zhou, J. Liang, H.X. Hao, C. Lu, A modified layer-removal method for residual stress measurement in electrodeposited nickel films, *Thin Solid Films* 519 (2011) 3249.
- [27] C. Krauss, S. Labat, S. Escoubas, O. Thomas, S. Carniello, J. Teva, F. Schrank, Stress measurements in tungsten coated through silicon vias for 3D integration, *Thin Solid Films* 530 (2013) 91.
- [28] S. Timoshenko, *History of Strength of Materials*, McGraw-Hill, Cambridge, U.K., 1953.
- [29] D. Kiener, C. Motz, M. Rester, M. Jenko, G. Dehm, FIB damage of Cu and possible consequences for miniaturized mechanical tests, *Mater. Sci. Eng. A* 459 (2007) 262.
- [30] J.J. Wortman, R.A. Evens, Young's modulus, shear modulus, and Poisson's ratio in silicon and germanium, *J. Appl. Phys.* 36 (1965) 153.
- [31] M.A. Hopcroft, W.D. Nix, T.W. Kenny, What is the Young's modulus of silicon? *J. Microelectromech. Syst.* 19 (2010) 229.
- [32] K. Matoy, H. Schönherr, T. Detzel, T. Schöberl, R. Pippan, C. Motz, G. Dehm, A comparative micro-cantilever study of the mechanical behavior of silicon based passivation films, *Thin Solid Films* 518 (2009) 247.
- [33] S.W. Bedell, A. Reznicek, K. Fogel, J. Ott, D.K. Sadana, Strain and lattice engineering for Ge FET devices, *Mater. Sci. Semicond. Process.* 9 (2006) 423.
- [34] C. Mendibide, P. Steyer, C. Esnouf, P. Goudeau, D. Thiaudière, M. Gailhanou, J. Fontaine, X-ray diffraction analysis of the residual stress state in PVD TiN/CrN multilayer coatings deposited on tool steel, *Surf. Coat. Technol.* 200 (2005) 165.
- [35] T. Kitamura, H. Hirakata, T. Itsuji, Effect of residual stress on delamination from interface edge between nano-films, *Eng. Fract. Mech.* 70 (2003) 2089.
- [36] J. An, Q.Y. Zhang, Structure, morphology and nanoindentation behavior of multilayered TiN/TaN coatings, *Surf. Coat. Technol.* 200 (2005) 2451.
- [37] H.C. Barshilia, B. Deepthi, A.S. Arun Prabhu, K.S. Rajam, Superhard nanocomposite coatings of TiN/Si<sub>3</sub>N<sub>4</sub> prepared by reactive direct current unbalanced magnetron sputtering, *Surf. Coat. Technol.* 201 (2006) 329.
- [38] Z. Novotná, R. Králová, R. Novák, J. Marek, X-ray analysis of residual stresses in TiN coatings, *Surf. Coat. Technol.* 116–119 (1999) 424.
- [39] P.H. Mayrhofer, M. Geier, C. Löcker, L. Chen, Influence of deposition conditions on texture development and mechanical properties of TiN coatings, *Int. J. Mater. Res.* 100 (2009) 1052.
- [40] E. Harry, A. Rouzaud, M. Ignat, P. Juliet, Mechanical properties of W and W(C) thin films: Young's modulus, fracture toughness and adhesion, *Thin Solid Films* 332 (1998) 195.
- [41] A. Rouzaud, E. Barbier, J. Ernoult, E. Quesnel, A method for elastic modulus measurements of magnetron sputtered thin films dedicated to mechanical applications, *Thin Solid Films* 270 (1995) 270.
- [42] H.L. Sun, Z.X. Song, D.G. Guo, F. Ma, K.W. Xu, Microstructure and mechanical properties of nanocrystalline tungsten thin films, *J. Mater. Sci. Technol.* 26 (2010) 87.
- [43] S. Wurster, C. Motz, M. Jenko, R. Pippan, Micrometer-sized specimen preparation based on ion slicing technique, *Adv. Eng. Mater.* 12 (2010) 61.
- [44] Simulia, Abaqus Documentation, Dassault Systemes Simulia Austria GmbH, [http://www.simulia.com/products/abaqus\\_fea.html](http://www.simulia.com/products/abaqus_fea.html) 2013.
- [45] K. Levenberg, A method for the solution of certain problems in least squares, *Q. Appl. Math.* 2 (1944) 164.
- [46] D. Marquardt, An algorithm for least-squares estimation of nonlinear parameters, *J. Appl. Math.* 11 (1963) 431.
- [47] M. Stefanelli, J. Todt, A. Riedl, W. Ecker, T. Müller, R. Daniel, M. Burghammer, J. Keckes, X-ray analysis of residual stress gradients in TiN coatings by a Laplace space approach and cross-sectional nanodiffraction: a critical comparison, *J. Appl. Crystallogr.* 46 (2013) 1378.
- [48] M.J. Bamber, K.E. Cooke, A.B. Mann, B. Derby, Accurate determination of Young's modulus and Poisson's ratio of thin films by a combination of acoustic microscopy and nanoindentation, *Thin Solid Films* 398–399 (2001) 299.
- [49] S.-H. Kim, Determination of mechanical properties of electroplated Ni thin film using the resonance method, *Mater. Lett.* 61 (2007) 3589.
- [50] Z. Huang, G. Leighton, R. Wright, F. Duval, H.C. Chung, P. Kirby, R.W. Whatmore, Determination of piezoelectric coefficients and elastic constant of thin films by laser scanning vibrometry techniques, *Sensors Actuators A Phys.* 135 (2007) 660.
- [51] J. Zhang, Determination of Young's modulus of electroplated nickel-iron (Ni/Fe) and micro-machined Si thin films by the balance method, *J. Mater. Process. Technol.* 123 (2002) 329.
- [52] J.M. Antunes, J.V. Fernandes, N.A. Sakharova, M.C. Oliveira, L.F. Menezes, On the determination of the Young's modulus of thin films using indentation tests, *Int. J. Solids Struct.* 44 (2007) 8313.
- [53] M.D. Tran, J. Poublan, J.H. Dautzenberg, A practical method for the determination of the Young's modulus and residual stresses of PVD thin films, *Thin Solid Films* 308–309 (1997) 310.